Experimental and numerical investigations of hybrid high strength steel welded T-section stub columns with Q690 flange and Q460 web

Jun-zhi Liu[1]; Shuxian Chen[1]; Tak-Ming Chan[1,2 *]

[1] Department of Civil and Environmental Engineering, The Hong Kong Polytechnic University, Hong Kong, China

[2] Chinese National Engineering Research Centre for Steel Construction (Hong Kong Branch), The Hong Kong Polytechnic University, Hong Kong, China

* Corresponding author: tak-ming.chan@polyu.edu.hk

Abstract

Comprehensive experimental and numerical investigations on mechanical properties of Q690 and Q460 high strength steel (HSS) materials and stub column behaviour of the 14 hybrid HSS welded T-section stub column specimens are presented in this paper. A total of six coupon specimens were longitudinally and transversely machined from HSS Q690 and Q460 steel parent plates respectively. Furthermore, initial local geometric imperfections measurements were also carried out. In parallel with the experimental investigation on stub column behaviour, extensive numerical studies were carried out by developing finite element (FE) models to replicate the experimental tests results. The validation of the FE models was confirmed against the obtained experimental data. To supplement the experimental data, validated FE models were used in the parametric studies, by which numerical specimens with a larger range of cross-section dimensions can be generated. Subsequently, cross-section classification slenderness limits for outstand plate elements under compressive load set out in structural steel design codes of EN 1993-1-12, ANSI/AISC 360-16, AS 4100 were evaluated against the experimental and numerical data. In addition to the design codes, design methods such as direct strength method (DSM) and continuous strength method (CSM) were also assessed to evaluate the applicability and suitability for hybrid HSS welded T-section stub columns. It was found that the current codified slenderness limits in EN 1993-1-12, ANSI/AISC 360-16 as well as AS 4100 for slender/non-slender outstand flat elements can generally be adopted for hybrid HSS welded T-section under compression. CSM provide under-estimated compressive resistance in comparison to the design codes and DSM for slender sections.

Keywords: Hybrid steel stub column; Local buckling behaviour; High strength steel; Finite element modelling; Design analysis.

1. Introduction

High strength steel (HSS) sections with nominal yield strength greater than 460 MPa, exhibit relatively high strength-to-weight ratio, resulting in reduced cross section dimensions, light-weight structures as well as reduced consumption of non-renewable resources [1]. Those advantages make HSS sections favourable in long-span structures and high-rise buildings. Experimental and numerical investigations have been previously conducted on various types of cross sections for HSS stub columns. Nishino et al. [2] and Nishino and Tall [3] carried out HSS welded sections with nominal yield strength of 690 MPa. Rasmussen and Hancock [4] executed welded box sections with nominal yield strength of 690 MPa to study the cross-sectional behaviour. High strength steel welded box sections with nominal yield strength higher than 460 MPa was also investigated by Shi et al. [5].

It was observed that most existing experimental investigations focused on high strength steel with the doubly symmetric section such as box-section and I-section. Some experimental investigations on non-doubly symmetric sections were conducted to examine the local buckling behaviour and cross-section capacities for channel and angle sections. Experimental investigations for angle sections and channel sections have been studied by Zhang et al. [6] and Wang et al. [7] with nominal yield strength up to 690 MPa and 960 MPa. Cao et al. [8] conducted experimental and numerical analyses on HSS T-section columns with nominal yield strength up to 800 MPa. Local buckling behaviour and cross-section resistance were investigated by Liu et al. [9] for HSS T-section stub columns with nominal yield strength of 690 MPa. In addition to experimental investigation on HSS sections, the application of hybrid sections is gaining increasing interests. The concept of hybrid sections has been applied to structural members such as columns in [10] and beams [11–13]. The hybrid sections are special types of structural members that consist of higher strength steel flange and lower strength steel web. Hybrid sections can effectively resist the load by placing higher strength materials in a position where higher stresses are introduced. Ito et al. [14] experimentally investigated the local buckling capacity of HSS hybrid section with the flange produced from SM570Q steel (nominal yield strength = 460MPa) and web made from SM 400 steel (nominal yield strength = 235MPa). The experimental study demonstrated that the hybrid sections practically have better deformation capacity than their homogeneous counterparts which are made up of the higher strength grade. Experimental investigation on hybrid cross sections to examine the flexure behaviour of the welded I-section at cross-sectional level were also conducted by Wang et al. [15]. The ductility of the hybrid cross section decreases as the strength of the flange increases using the same geometric dimensions. Bartsch et al. [16] conducted experimental and numerical studies on local buckling behaviour of homogeneous and hybrid I-section beams. The homogeneous I-section beams were made from S690 steel and hybrid I-section beams comprised S690 flange and S355 web.

Well-understanding of the interactions between the constituent plates is necessary for application and analysis for hybrid sections. It is known that hybrid sections are more efficiently utilized for members under flexural loads with stress gradients such as beams and beam-columns. However, investigating the local buckling behaviour and cross-section strength under pure compression is very crucial, as it provides fundamental understanding under the worst loading condition which can pave the way for further analysis of the structural behaviour under bending and combined compression and bending. In addition, the applicability of the current design codes to the HSS hybrid T-sections under pure compression is unknown and no research has been performed to examine the interaction effect and the cross-section behaviour of hybrid HSS welded T-section stub columns. Moreover, the current structural steel design specifications EN 1993-1-12 [17] and ANSI/AISC-360-16 [18] generally extend the codified contents specifying for conventional steels. The suitability of these design specifications on hybrid sections should be compared and assessed. The aim of this paper is to study the local buckling behaviour and the cross-sectional capacities of hybrid HSS welded T-section stub columns. Aligned with the compressive loading test for fourteen stub column specimens, the material properties of the steel plates fabricating the hybrid cross sections were tested through tensile coupon tests. The tensile coupon specimens were extracted from parent steel plates with different thicknesses and strength grades. Initial local geometric imperfection measurements were also carried out. The finite element (FE) models were developed based on the obtained test results, after which extensive parametric studies were subsequently performed covering a wider spectrum of cross-section geometries. Experimental data integrating with the numerical data from parametric studies were used to assess the strength predictions and applicability of the current design specifications for structural steel including EN 1993-1-12 [17], ANSI/AISC-360-16 [18] as well as the design

method of Direct Strength Method (DSM) [19] and Continuous Strength Method (CSM) [20] which can effectively take account of the element interactions.

2. Experimental investigation

2.1. Test specimens

A total of 14 hybrid HSS welded T-section stub columns tests were tested at the Structural Engineering Research Laboratory of The Hong Kong Polytechnic University. The examined hybrid HSS welded T-sections in this study comprised flanges fabricated from Q690 steel plates and webs fabricated from Q460 steel plates. The high strength steel plates Q690 and Q460 were delivered in Quenched and Tempered (QT) conditions with chemical composition shown in Table 1 and Table 2 for Q690 and Q460 HSS materials respectively. The HSS hybrid T-section stub columns were fabricated by gas metal arc welding (GMAW) with the electrode in the category of ER80S-G. The detailed chemical compositions of the selected electrode are presented in Table 3. Fig. 1 shows the definition of the geometric symbols of the cross sections, where H is the height of the cross section, B is the width of the flange, h_w is the clear width of the web, b_f is the clear width of the flange. A specimen labelling system was used in this study, with the letter "T" representing the welded T-sections, "HSC" indicating the hybrid stub column specimen and the nominal dimensions of ($H \times t_w$, in mm) following after the hyphen. The symbol of "#" was used to indicate the repeated test specimen. For example, T-HSC-120 × 6# indicates a repeated hybrid HSS welded T-section specimen with nominal overall height of 120 mm and with the nominal web thickness of 6 mm. The actual dimensions of the hybrid HSS welded hybrid T-sections were measured prior to the compressive tests which are summarized in Table 4.

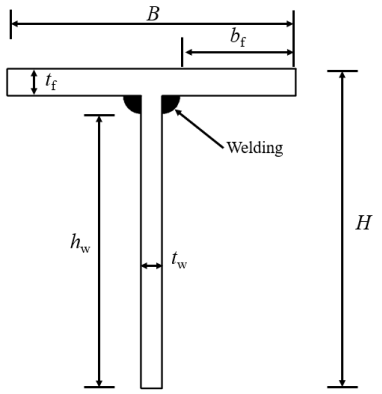

Fig. 1. Notations of the HSS hybrid welded T-section

Table 1 Chemical compositions listed in mill certificate for 10 mm thick Q690 parent plate.

Steel plate	Chemical composition (wt%)										
	C	Mn	P	S	Si	Cr	Mo	Nb	Ti	B	CEV
10 mm plate	0.14	1.40	0.019	0.001	0.27	0.26	0.15	0.024	0.013	0.002	0.46

Table 2 Chemical compositions listed in mill certificate for 6 mm thick Q460 parent plate.

Steel plate	Chemical composition (wt%)									
	C	Mn	P	S	Si	Cr	Nb	Ti	V	CEV
6 mm plate	0.08	1.43	0.013	0.003	0.15	0.33	0.023	0.011	0.002	0.38

Table 3 Chemical compositions of the welding electrode ER80S-G.

Electrode	Chemical composition (wt%)										
	C	Mn	P	S	Si	Cr	Mo	Al	Cu	V	CEV
ER80S-G	0.10	1.40	0.005	0.003	0.70	0.03	0.02	0.02	0.10	0.03	0.36

Table 4 Measured geometric dimensions and initial local geometric imperfections of hybrid HSS welded T-section stub column specimens.

Specimens	L (mm)	B (mm)	H (mm)	b_f (mm)	h_w (mm)	t_f (mm)	t_w (mm)	ω_0 (mm)
T-HSC-50 × 6	200	109.2	49.9	43.2	32.0	9.61	6.14	0.16
T-HSC-60 × 6	200	109.4	60.2	43.1	42.0	9.62	6.13	0.18
T-HSC-70 × 6	200	109.6	70.7	42.5	51.9	9.61	6.13	0.21
T-HSC-75 × 6	200	109.3	75.9	44.7	59.4	9.60	6.12	0.24
T-HSC-80 × 6	300	109.5	79.9	44.3	62.9	9.60	6.15	0.23
T-HSC-80 × 6#	300	109.4	79.8	44.1	62.7	9.61	6.13	0.19
T-HSC-90 × 6	300	109.5	91.5	43.1	73.3	9.63	6.13	0.25
T-HSC-100 × 6	300	109.4	100.2	44.0	82.9	9.62	6.14	0.17
T-HSC-100 × 6#	300	109.4	100.1	43.8	82.7	9.61	6.13	0.16
T-HSC-120 × 6	400	109.5	120.2	43.7	102.6	9.60	6.13	0.21
T-HSC-150 × 6	400	109.6	150.6	44.3	133.6	9.62	6.14	0.22
T-HSC-170 × 6	450	109.5	170.4	43.7	152.8	9.63	6.12	0.24
T-HSC-180 × 6	450	109.4	180.6	42.4	161.7	9.62	6.13	0.18
T-HSC-200 × 6	525	109.5	199.8	43.9	182.4	9.60	6.12	0.20

Note: # indicates a repeated test

2.2. Material properties

To obtain the material properties of the parent plates used to manufacture the hybrid HSS T-section stub columns, tensile coupon specimens were taken to determine the corresponding material properties for Q690 parent steel plate and Q460 parent steel plate respectively. To ensure the homogeneous material properties of the HSS steel plates, the tensile coupon specimens were machined from the parent steel plates along longitudinal and transverse directions. A total of six coupon specimens were taken from each parent steel plate. The dimensions of the coupon specimens were carefully determined in accordance with ISO EN 6892-1: 2019 [21]. Tensile tests were conducted using Instron 5982, an electro-mechanical high force universal testing system, which can provide a capacity of 100 kN. The arrangement and test set-up of the tensile coupon test is

shown in Fig. 2. An optical non-contact video extensometer was adopted to obtain the engineering stress-strain relationship with gauge length of either 25 mm or 50 mm which can be customized by the user through painting the white dots. Concerning the tensile load application, displacement load-control was employed with an initial loading speed of 0.05 mm/min up to the yield strength and the loading speed was changed to 0.1 mm/min beyond yield strength to speed up the process but maintaining a low speed to mimic the static loading [22–23]. Two strain gauges were affixed to both sides at the mid-height of the coupon specimens, based on which the elastic modulus and the average strain can be determined. Typical stress-strain curves of the parent plates are plotted in Fig. 3 and Fig. 4 for 6 mm thick Q460 and 10 mm thick Q690 parent plates respectively. The measured properties of the parent plates are summarized in Tables 5 – 6 for 6 mm and 10 mm thick parent plates respectively, where E_s indicates the elastic modulus, f_y is yield strength, f_u is the ultimate strength, ε_{sh} is strain-hardening strain, ε_u is strain at ultimate strength, ε_f is proportional elongation at fracture.

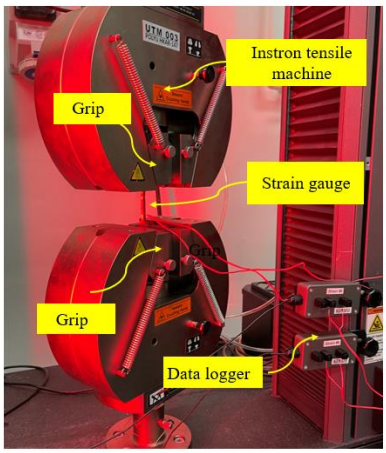

Fig. 2 Test arrangement of the tensile coupon specimen

Table 5 Measured material stress–strain curves from longitudinal and transverse coupons from 6 mm thick Q460 parent plate.

Section	E_s (GPa)	f_y (MPa)	f_u (MPa)	ε_u (%)	ε_f (%)	ε_{sh} (%)
6 mm plate-L1	213.6	516	649	14.0	27.5	1.39
6 mm plate-L2	212.5	516	652	14.6	28.6	1.39
6 mm plate-L3	217.8	510	640	13.7	30.9	1.45
Mean	214.6	514	647	14.1	29.0	1.41
CoV	0.011	0.006	0.008	0.027	0.049	0.020
6 mm plate-T1	217.1	521	665	13.8	27.2	1.15
6 mm plate-T2	217.3	519	661	13.5	28.3	1.16
6 mm plate-T3	213.0	522	664	13.6	28.4	1.08
Mean	215.8	521	663	13.6	28.0	1.13
CoV	0.009	0.002	0.003	0.009	0.019	0.031

Table 6 Measured material stress–strain curves from longitudinal and transverse coupons from 10 mm thick parent plate.

Section	E_s (GPa)	f_y (MPa)	f_u (MPa)	ε_u (%)	ε_f (%)	ε_{sh} (%)
10 mm plate-L1	214.8	812	839	6.8	18.7	3.48
10 mm plate-L2	213.9	818	846	6.8	18.4	3.48
10 mm plate-L3	219.5	815	844	6.5	18.2	3.61
Mean	216.1	815	843	6.7	18.4	3.52
CoV	0.011	0.003	0.003	0.021	0.011	0.017
10 mm plate-T1	219.0	824	853	6.9	17.8	3.49
10 mm plate-T2	216.8	817	845	6.3	18.4	3.45
10 mm plate-T3	216.3	817	847	7.0	18.8	3.31
Mean	217.4	819	848	6.7	18.3	3.42
CoV	0.005	0.004	0.004	0.046	0.022	0.023

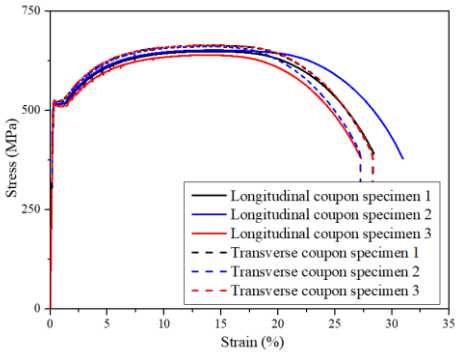

Fig. 3 Measured material stress–strain curves of Q460 high strength steel longitudinal and transverse tensile coupons extracted from 6 mm thick parent plate

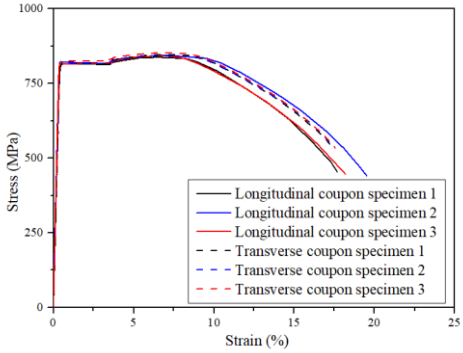

Fig. 4 Measured stress–strain curves of Q690 high strength steel longitudinal and transverse tensile coupons of 10 mm thick parent plate

2.3 Initial local geometric imperfection measurements

Initial local geometric imperfections have negative impact on the bearing resistance of the thin-walled structural elements, which can be induced during the manufacturing process or transportation. In this investigation, the measurements of the initial local imperfections were carried out for each hybrid HSS welded T-section stub column. Linear Variable Displacement Transducers (LVDTs) with an accuracy of 0.001 mm were used. A set of three LVDTs was affixed to the head of the milling machine by specially developed fixtures which can move longitudinally along the length of the specimen. The set-up of the initial imperfection measurement such as the LVDTs arrangement of the measurement as well as the sign conventions of the measured local imperfection are shown in Fig. 5. The hybrid HSS welded T-section stub column was mounted on a milling machine which works as a measuring platform. Each surface of the specimens was measured with two LVDTs located near the sides and one at the mid portion of the constituent plate element. Measurement was taken at a 2 mm interval along the specimen length. The same configurations of the imperfection measurements have been adopted in [24, 25]. To eliminate the potential local imperfection caused by plate cutting at the side and the end of the plate, the measurements were started and terminated at the location 20 mm away from each end of the specimen. The magnitude of initial local geometric imperfection of the plate elements was taken to be the deviation between the measurements at the mid-portion and a straight datum line connecting the measurements at the sides. A typical measured geometric imperfection profile of the HSS hybrid welded T-section is presented in Fig. 6. The measured maximum amplitudes (ω_0) of the local geometric imperfection for each specimen is given in Table 4.

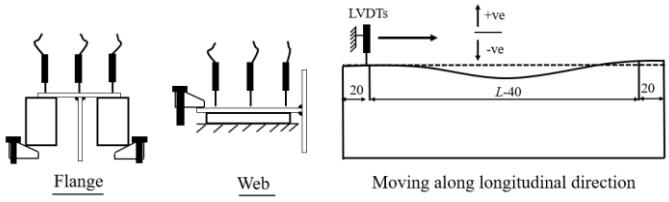

(a) Schematic view

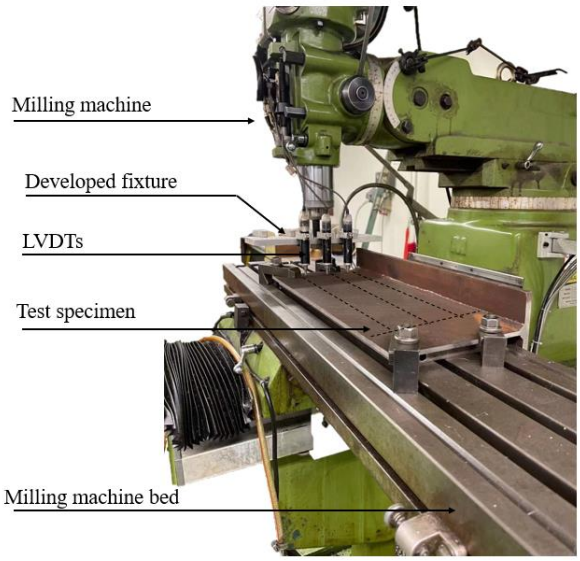

(b) Experimental arrangement

Fig. 5 Setup of local geometric imperfection measurements for HSS hybrid welded T-section.

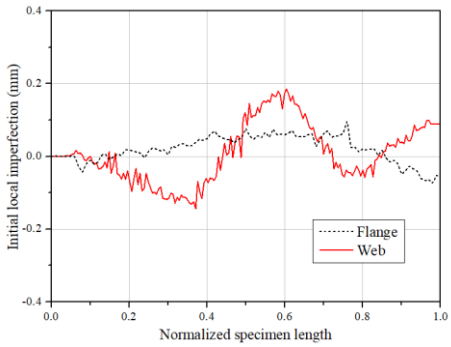

Fig. 6. Measured initial local geometric imperfection measurements for HSS hybrid welded T-section T-HSC-60 × 6.

2.4 Stub column tests

To investigate the local buckling behaviour and the cross-sectional resistances for hybrid HSS welded T-section stub columns, 14 stub column specimens were executed under concentric compressive load. To ensure the applied load can be uniformly distributed and the good contact between the end plates and the stub column specimen, the ends of all the specimens were milled flat. To prevent the premature local buckling failure at the section ends due to the highly concentrated loads, a pair of the specially developed end clampers, comprising a number of high strength bolts, were designed, as shown in Fig. 7. The compressive loading test was conducted by using an MTS machine with capacity of 5000 kN. The test set-up comprised four 50 mm range LVDTs to measure the end shortening of the stub columns, as shown in Fig. 7. For the purpose of eliminating the possible gaps between the specimen and the bearing end plate, an initial load of approximately 10 kN was applied to the specimens. Strain gauges with locations shown in Fig. 7 were adhered to the mid-height of the test specimens to record the compressive strain. Displacement control was applied to the stub column specimens with a constant loading rate of 0.2 mm/min. Note that the data from LVDTs invariably include the elastic deformations from end plates and specimens. It is thereby necessary to obtain the true end shortening of the specimen by excluding the elastic deformation from the end plates. Readings from the strain gauges were used to determine the true end shortening [26, 27]. The obtained load-end shortening curves of the tested hybrid HSS welded T-section stub columns are presented in Fig. 8. Key test results are summarized in Table 7 including the ultimate axial load $N_{u,test}$, the end shortening at ultimate load δ_u, yield load N_y and the ultimate to yield load ratio $N_{u,test}/N_y$. It should be noted that the yield load of N_y was determined based on the equivalent yield strength $f_y^* \times A$, which equals to $(A_{,f} \times f_{y,f} + A_{,w} \times f_{y,w})/(A_{,f} + A_{,w})$, where $f_{y,f}$ is the 0.2% proof strength of the flange and $f_{y,w}$ is the 0.2% proof strength of the web, $A_{,f}$ and $A_{,w}$ are the area of flange and web respectively. Meanwhile, the comparisons between the test results and the predicted bearing capacities from numerous design codes with statistical analysis results are also presented. For the stub column specimens with the ratio of $N_{u,test}/N_y$ lower than the unity were failed by local buckling whereas the stub column specimens experienced yielding failure if the ratio N_u/N_y is higher than the unity. The load-strain curves of the hybrid HSS welded T-section stub column is plotted in Fig. 9. The compressive strains consistently increase under the axial compressive load for all strain gauges in early elastic stage. After the occurrence of local buckling, the compressive strains corresponding to the buckling location start to decrease, and the dashed cross implies local

buckling load as shown in Fig. 9. Typical local buckling mode with plate buckling was observed for all the test stub columns. Fig. 10 shows some of the failed stub column specimens with representative failure modes.

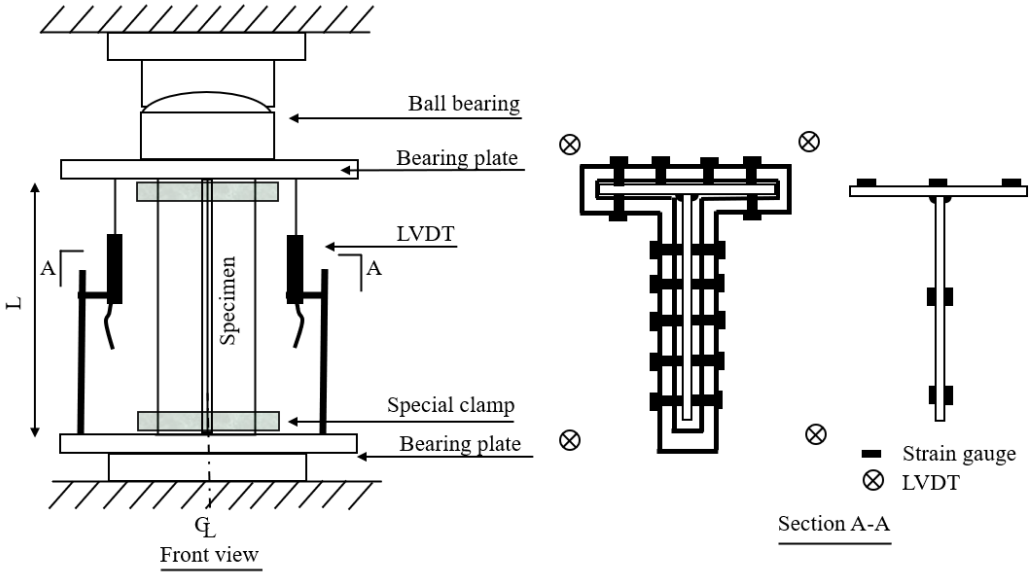

(a) Schematic arrangement

(b) Experimental arrangement

Fig. 7 Test set-up for HSS hybrid welded T-section stub column

Table 7 Summary of hybrid HSS welded T-section stub column test results.

Specimens	$N_{u,test}$ (kN)	δ_u (mm)	$N_{u,test}/Af_y^*$	$N_{u,test}/N_{u,EC3}$	$N_{u,test}/N_{u,AISC}$	$N_{u,test}/N_{u,AS4100}$	$N_{u,test}/N_{u,DSM}$	$N_{u,test}/N_{u,DSM}^*$	$N_{u,test}/N_{u,CSM}$	$N_{u,test}/N_{u,CSM}^*$
T-HSC-50 × 6	1025.6	3.86	1.04	1.04	1.04	1.04	1.04	1.04	1.02	1.03
T-HSC-60 × 6	1061.2	4.21	1.04	1.04	1.04	1.04	1.04	1.04	1.01	1.03
T-HSC-70 × 6	1092.4	3.86	1.04	1.04	1.04	1.04	1.04	1.04	1.02	1.03
T-HSC-75 × 6	1088.5	3.13	1.02	1.02	1.02	1.02	1.02	1.02	1.00	1.02
T-HSC-80 × 6	1108.0	2.81	1.02	1.03	1.02	1.03	1.02	1.02	1.02	1.02
T-HSC-80 × 6#	1107.1	2.85	1.02	1.03	1.02	1.03	1.02	1.02	1.02	1.02
T-HSC-90 × 6	1128.5	2.76	1.01	1.04	1.01	1.05	1.01	1.01	1.01	1.07
T-HSC-100 × 6	1142.5	2.83	0.99	1.05	1.02	1.06	0.99	1.03	1.00	1.11
T-HSC-100 × 6#	1140.7	2.81	0.99	1.05	1.02	1.06	0.99	1.03	1.00	1.11
T-HSC-120 × 6	1164.4	2.45	0.96	1.06	1.02	1.08	1.02	1.17	1.10	1.27
T-HSC-150 × 6	1166.1	2.54	0.89	1.05	1.01	1.08	1.08	1.25	1.18	1.39
T-HSC-170 × 6	1192.3	1.87	0.87	1.07	1.02	1.11	1.18	1.36	1.31	1.56
T-HSC-180 × 6	1195.6	2.25	0.85	1.07	1.02	1.11	1.20	1.39	1.34	1.60
T-HSC-200 × 6	1206.8	2.31	0.82	1.09	1.03	1.12	1.25	1.45	1.41	1.69
			Mean	1.05	1.02	1.06	1.06	1.13	1.10	1.21
			CoV	0.017	0.009	0.030	0.075	0.136	0.127	0.196

Note: # indicates a repeated test; f_y^* is the equivalent yield strength which equals to $(A_{,f} \times f_{y,f} + A_{,w} \times f_{y,w})/(A_{,f} + A_{,w})$, where $f_{y,f}$ is the 0.2% proof strength of the flange and $f_{y,w}$ is the 0.2% proof strength of the web, $N_{u,DSM}^*$ is the compressive resistance calculated based on $\lambda_p = (f_{cr}/f_{y,f})^{0.5}$ whereas $N_{u,DSM}$ is the compressive resistance calculated based on $\lambda_p = (f_{cr}/f_{y,w})^{0.5}$. Similarly, $N_{u,CSM}^*$ is the predicted compressive resistance calculated based on $\lambda_p = (f_{cr}/f_{y,f})^{0.5}$ and $N_{u,CSM}$ is the predicted compressive resistance calculated based on $\lambda_p = (f_{cr}/f_{y,w})^{0.5}$.

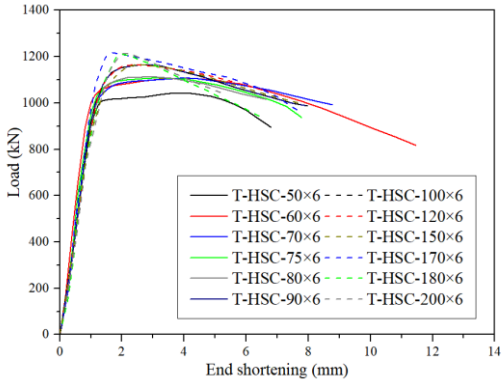

Fig. 8. Load-end shortening curves of hybrid HSS welded T-section stub columns

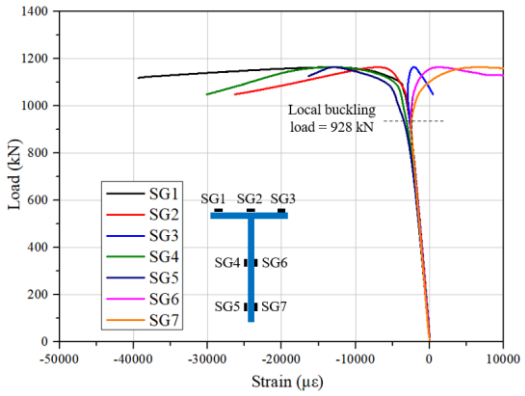

Fig. 9. Load-strain curves of hybrid HSS welded T-section stub column specimen of T-HSC-120 × 6

Fig. 10. Experimental failure modes of the representative HSS hybrid welded T-section stub columns

3. Numerical investigation

3.1 Finite element modelling

In conjunction with the experimental investigations, numerical investigations were also carried out to develop and validate the finite element models and conduct the parametric studies with generated data covering larger range of dimensions. To build the FE models, the measured cross-section dimensions and lengths were used for each stub column specimen. For the input of mechanical properties, the mean Young's modulus, yield strength as well as ultimate strength were employed and converted to true stress and true plastic strain.

A four-node shell element S4R with reduced integration was applied in FE model which has been successfully applied in previous investigations [30, 31]. Mesh sensitivity study was carried out with element size varying from 0.5t to 3.0t. The results indicated that an element size equal to the thickness t can provide good balance between numerical accuracy and computational costs. Further to the boundary conditions of the FE models, all degree of freedom of the end sections of the stub columns were fully restrained except for the axial translation.

Linear elastic buckling analysis was performed prior to the non-linear buckling analysis. The lowest elastic buckling eigen mode under compression was taken as the representative distributed profile of initial local geometric imperfection which was subsequently multiplied by the measured imperfection value to the amplitude of the corresponding eigen mode as shown in Fig. 11. To evaluate the sensitivity of the developed FE models to the imperfection magnitudes, four imperfection magnitudes, namely the measured local geometric imperfection value ω_0, and three investigated imperfection values expressed by the fraction of the web plate thickness (t_w/10, t_w/50, t_w/100) were included in FE models. Mean values of $N_{u,FE}/N_{u,test}$ of the four considered initial local imperfection magnitudes are 1.00, 0.99, 0.99 and 1.00 respectively with corresponding CoVs of 0.022, 0.022, 0.024 and 0.024 as shown in Table 8. It was found that the measured imperfection magnitudes provide the best agreement with the test observations. Based on the sensitivity studies of the imperfections as shown in Table 8, it is observed that the ultimate strength predictions from the FE simulations were relatively insensitive to the variations of the magnitude of the initial local geometric imperfections. Among the investigated imperfection magnitudes, magnitude of t_w/10 provide comparable but conservative predictions compared with measured imperfection magnitudes, thus this imperfection value was used as it can provide reliable predictions in later parametric study in sub-section 3.3.

Compressive load was applied to the FE model by specifying the axial displacement through RIKS step. The non-linear geometric command was activated to allow for large displacement analysis. Membrane residual stress is caused mainly due to the heat input and the uneven cooling during the welding process [32,33]. During the process of cooling down after welding the two steel plates, the elongation of the heated zone along the welded direction is restricted by the adjacent unheated zone, resulting in the tensile membrane residual stresses interlocked in the members. The membrane residual stress distribution for HSS T-section proposed in [34] was incorporated in FE models with command of "INITIAL CONDITIONS" activated. To account for the fillet weld geometries, additional shell elements with varying thicknesses were added to the junction between the flange and the web, as shown in Fig. 12. The material properties of these elements were assumed to be the same as those of the web, which have been successfully applied in [28,29].

Similar distribution pattern of the residual stress in hybrid sections and homogeneous sections are found in Nagarajarao et al. [9] and Kang et al. [43]. Nagarajarao et al. [9] observed that hybrid sections exhibit

comparable lower residual stress compared with the homogeneous sections. Thus, incorporating the membrane residual stress distribution for homogeneous HSS T-section in Cao et al. [34] would give rational results due to the conservative consideration of the membrane residual stress., as shown in Fig. 13. The residual stresses equilibrium was satisfied in the components of web and flange plates in FE models with total net force equal to zero. A typical membrane residual stress distribution incorporated into the FE model for the hybrid HSS stub column specimen T-HSC-150 × 6 is presented in Fig. 14 with positive values indicating tensile membrane residual stress and negative values representing compressive membrane residual stress. To evaluate the influence of the membrane residual stress on the bearing capacity and the structural response of the stub column specimen, the FE model results taking account of the membrane residual stress were compared with the counterpart without the inclusion of membrane residual stress, as shown in Fig. 15. The comparison between the load-end shortening curves of the FE model with and without consideration of residual stress illustrates that the impact of the residual stress on the resistance capacity is minimal and it is within 3%. Therefore, the residual stresses were not modelled in the parametric studies.

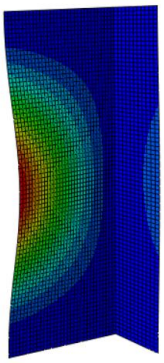

Fig. 11. The lowest eigen mode of HSS hybrid welded T-section stub columns from elastic buckling analysis

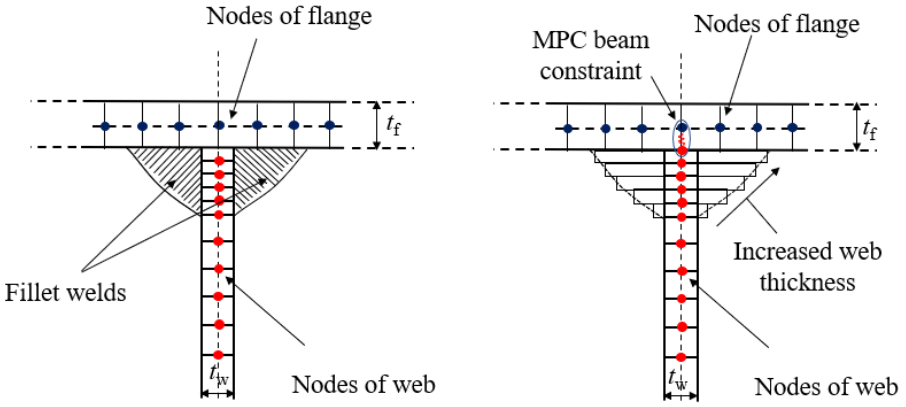

Fig. 12. FE modelling of the geometries of fillet welds in welded hybrid T-sections [9, 28, 29]

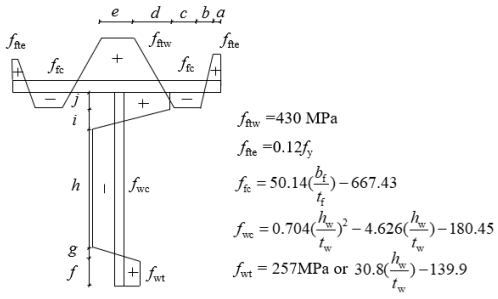

Fig. 13. Typical membrane residual stress distribution and amplitudes (in MPa) in modelled hybrid HSS welded T-section stub columns [34].

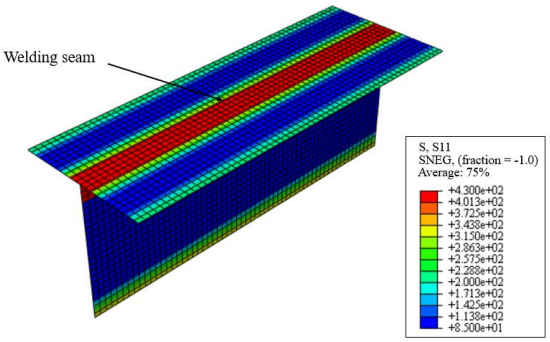

Fig. 14. Predictive model for membrane residual stress distribution in modelled hybrid HSS welded T-section stub columns T-HSC-150 × 6.

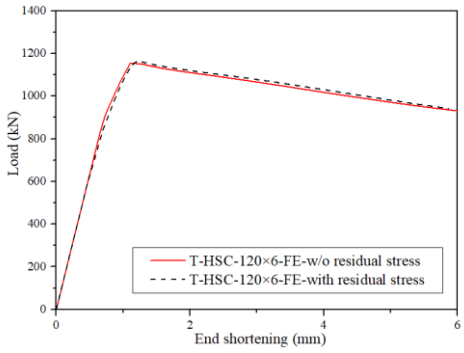

Fig. 15. Effect of membrane residual stress on hybrid HSS welded T-section stub column T-HSC-120 × 6

3.2 Validation of FE models

The developed FE models should be validated against the experimental results including the failure modes, ultimate resistance loads, and load-end shortening curves. Excellent agreement between the FE models and the test results can be observed as shown in Fig. 16, failure modes of the hybrid HSS welded T-section with inward and outward plate local buckling have been accurately replicated by the FE models. Regarding the load-end

shortening curves, Figs. 17(a) – 17 (c) present the comparisons between the experimental and numerical data for the specimen of T-HSC-60 × 6, T-HSC-120 × 6 and T-HSC-170 × 6 respectively. It was found that the numerical structural performance data correlated well with the experimental results. Based on the above information, it can be generally concluded that the developed FE models are capable of precisely replicating the failure modes, accurately predicting the ultimate compressive loads for hybrid HSS welded T-section stub column specimens.

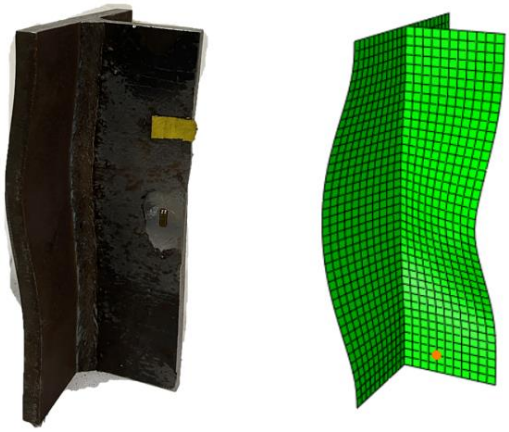

(a) HSS hybrid welded T-section stub column specimen T-HSC-60 × 6

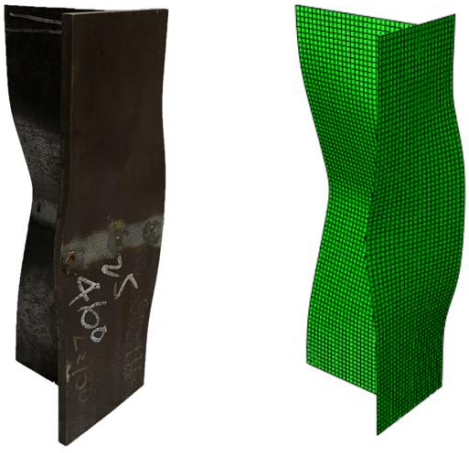

(b) HSS hybrid welded T-section stub column specimen T-HSC-120 × 6

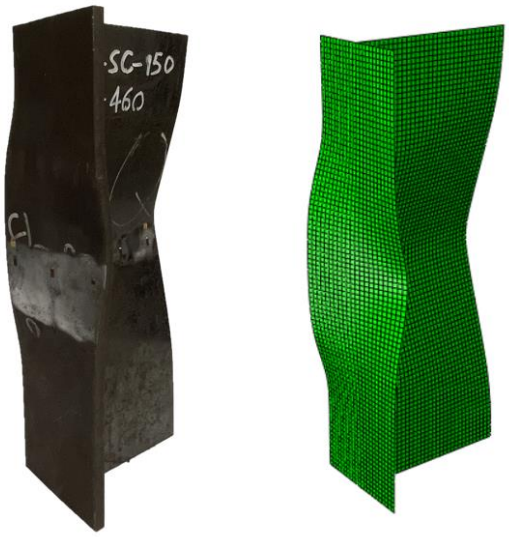

(c) HSS hybrid welded T-section stub column specimen T-HSC-150 × 6

Fig. 16. Test and FE failure modes for typical stub column specimens.

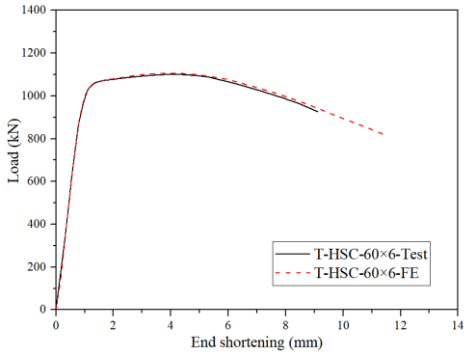

(a) Experimental and numerical load-end shortening responses of hybrid HSS welded T-section stub column T-HSC-60 × 6

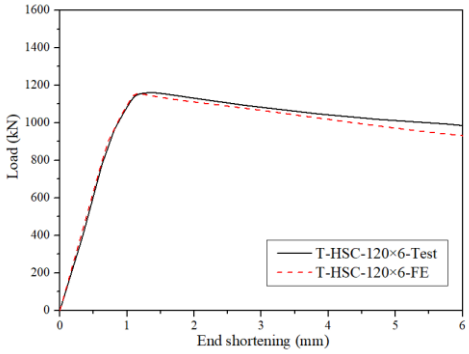

(b) Experimental and numerical load-end shortening responses of hybrid HSS welded T-section stub column T-HSC-120 × 6

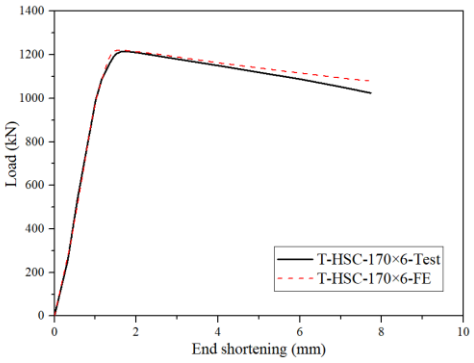

(c) Experimental and numerical load-end shortening responses of hybrid HSS welded T-section stub column T-HSC-170 × 6

Fig. 17. Comparisons between the experimental and numerical load-end shortening responses

3.3 Parametric studies

After validation, the validated hybrid HSS welded T-section sub column FE models were adopted to conduct numerical parametric studies to generate a wider range of cross-section dimensions complementing the experimental data. The material properties for flange and web were assigned with the corresponding mean material properties obtained from tensile coupon tests for Q690 and Q460 steel materials respectively. In terms of the geometric dimensions of the modelled hybrid T-section specimens, the width of the flanges was fixed at 110 mm, while the lengths of the web were varied from 53 mm to 206 mm, resulting in a large spectrum of cross section aspect ratios, as shown in Table 9. To minimize the effect of the thickness on the strength variation, the thicknesses of the web and flange are 6 mm and 10 mm respectively. The initial local imperfection with magnitude of $t_w/10$ was used as it generates closer predictions compared with $t_w/50$ and $t_w/100$, yet conservative prediction and same CoV with measured imperfection values. The length of the stub columns was determined as two times the outer cross-section depth. A total of 76 FE models were developed in the parametric studies. The parametric study results together with the test data were used to assess the current design provisions in the structural steel codes and the design methods of DSM and CSM.

Table 8 Comparison of the stub column test results with finite element results for various imperfection amplitudes.

Specimens	$N_{u,FE}/N_{u,test}$			
	ω_0	$t_w/10$	$t_w/50$	$t_w/100$
T-HSC-50 × 6	0.99	0.98	0.99	1.00
T-HSC-60 × 6	0.98	0.97	0.97	0.98
T-HSC-70 × 6	0.99	0.98	0.98	0.99
T-HSC-75 × 6	0.97	0.96	0.96	0.97
T-HSC-80 × 6	0.96	0.95	0.95	0.96
T-HSC-80 × 6#	1.00	0.99	0.99	1.00
T-HSC-90 × 6	1.00	0.99	0.99	1.00
T-HSC-100 × 6	0.99	0.98	0.98	0.99
T-HSC-100 × 6#	0.99	0.98	0.98	0.99
T-HSC-120 × 6	1.02	1.00	1.01	1.02
T-HSC-150 × 6	1.03	1.01	1.02	1.03
T-HSC-170 × 6	1.02	1.01	1.02	1.03
T-HSC-180 × 6	1.02	1.02	1.02	1.03
T-HSC-200 × 6	1.04	1.03	1.03	1.04
Mean	1.00	0.99	0.99	1.00
CoV	0.022	0.022	0.024	0.024

Note: # indicates a repeated test

Table 9 Cross-section geometric dimensions selected for parametric study.

B (mm)	t_w (mm)	t_f (mm)	H (mm)
110	6	10	53, 55, 57, 60, 62, 64, 66, 68, 70, 72, 74, 76, 78, 80, 82, 84, 86, 88, 90, 92, 94, 96, 98, 100, 102, 104, 106, 108, 110, 112, 114, 116, 118, 120, 122, 124, 126, 128, 130, 132, 134, 136, 138, 140, 142, 144, 146, 148, 150, 152, 154, 156, 158, 160, 162, 164, 166, 168, 170, 172, 174, 176, 178, 180, 182, 184, 186, 188, 190, 192, 194, 196, 198, 200, 202, 204, 206

4. Evaluation of the current design codes and design approaches

4.1. Overview

In this section, the suitability of the design provisions in design codes and design methods against 14 experimental data and 76 FE results for hybrid HSS welded T-sections were assessed and compared. Three structural steel design codes, viz, the European code EN 1993-1-12 [17], North American specification ANSI/AISC 360-16 [18] as well as Australian standard AS 4100 [35], were used for comparison and assessment for their applicability to hybrid HSS welded T-section stub columns.

4.2. Cross-section classification slenderness limits

To address the local buckling design of stub columns under compression, the concept of cross-section classification and the methodology of effective width method are used. Thus, slenderness limits for outstand flange of the welded section specified in EN 1993-1-12 [17] and AS 4100 [35] are assessed for hybrid sections. Note that Table B4.1a of ANSI/AISC 360-16 [17] provides the design provisions for T-section, but whether it can be applied to hybrid T-sections are unknown. Furthermore, the direct strength method (DSM) originally developed for the stability design of the sections taking account of the element interaction is assessed and the deformation-based design method, continuous strength method (CSM), taking account of the interaction effect and strain-hardening of the metallic material is also compared and discussed. There are four classes in the Eurocode classification framework, namely, Class 1, Class 2, Class 3 and Class 4 respectively. Class 1-3 sections are those sections that can achieve full yield load, whereas the Class 4 counterparts cannot reach the yield load due to elastic local buckling. For Class 4 sections, the reduced area A_{eff} is used to consider the ineffective buckling parts which can no longer resist the external loads, resulting in an effective compression resistance resultant $A_{\text{eff}}f_{\text{y}}$. In the classification framework of the EN 1993-1-12 [17], the classification of the cross sections solely depends on its slenderest constituent plate element and then being used to compare the width-to-thickness ratio c/t with codified slenderness limits, where c is the clear width of the plate element. Different material parameters such as $\varepsilon_{\text{EC3}} = (235/f_{\text{y}})^{0.5}$, $\varepsilon_{\text{AISC}} = (E/f_{\text{y}})^{0.5}$, and $\varepsilon_{\text{AS4100}} = (250/f_{\text{y}})^{0.5}$ are used to account for the differences of the material strengths in various codes respectively. The slenderness limits codified in those design codes for T-sections are given in Table 10. Compression resistances from experimental and numerical studies were used to normalize the corresponding squash load Af_{y}, and subsequently plotted against the ratios of $c/(t\varepsilon_{\text{EC3}})$, $c/(t\varepsilon_{\text{AISC}})$ and $c/(t\varepsilon_{\text{AS4100}})$ of the governing outstand flange of the T-sections in Figs. 18. In Fig. 18, comparisons generally demonstrate that the current codified slenderness limits in EN 1993-1-12 [17], ANSI/AISC 360-16 [18] as well as AS 4100 [35] for slender/non-slender outstand flat elements are safe and accurate for hybrid HSS welded T-section under compression.

In addition to the design codes, design methods such as DSM and CSM were developed to consider the interaction effect of the plate elements and eliminate the iterated work in calculating the effective width. To apply the DSM, governing buckling stress among elastic buckling, global buckling and distortional buckling stress should be derived through numerical software such as finite strip software CUFSM [42] or ABAQUS [37]. A non-dimensional cross-section slenderness parameter $\lambda_{\text{p}} = (f_{\text{y}}/f_{\text{cr}})^{0.5}$ is used in DSM where f_{y} is the yield strength of the steel material, f_{cr} is the elastic buckling stress. Note that the DSM for compressive member design has been included and detailed in Chapter E of the AISI-S100 [38]. For the sections with non-dimensional cross-section slenderness λ_{p} smaller than 0.776, the cross section can achieve the squash load.

Thus, the cross-section limit is 0.776 for DSM

Furthermore, design method of CSM was developed which can take the strain hardening behaviour of metallic material and plate element interaction into consideration [20, 28]. Calculating the effective area is not needed in CSM. The base curve forms the basis of CSM, which relates the deformation capacity $\varepsilon_{csm}/\varepsilon_y$ to the cross-section slenderness parameter $\lambda_p = (f_y/f_{cr})^{0.5}$ same as DSM. Base curves developed for HSS by Lan et al. [39] was used in this study, with expressions shown as follows in Eq. (1),

$$\begin{cases} \dfrac{\varepsilon_{csm}}{\varepsilon_y} = \dfrac{0.294}{\lambda_p^{3.174}} \le \min(15, \dfrac{C_1\varepsilon_u}{\varepsilon_y}) & \text{for } \lambda_p \le 0.68 \\ \dfrac{\varepsilon_{csm}}{\varepsilon_y} = (1 - \dfrac{0.219}{\lambda_p^{1.014}}) \dfrac{1}{\lambda_p^{1.014}} & \text{for } 0.68 < \lambda_p \end{cases} \quad (1)$$

where $\varepsilon_y = (f_y/E)$, and the constant C_1 and C_2 are the material related coefficients.

For the sections experiencing large deformation with strain hardening, CSM design stress of f_{csm} should be determined based on the strain hardening slope E_{sh} and the predicted strain ε_u corresponding to the ultimate stress are needed. To obtain these parameters, the expressions given in Eqs. (2) – (3) originally developed for hot-rolled steel by Yun and Gardner [40] and later modified to extend its application to HSS in [1] for nominal yield strength of 690 MPa and $f_y/f_u > 0.9$ as well as Q460 and $f_y/f_u \leqslant 0.85$ were used and assessed in this study, as shown in Table 11. It should be noted that the length of the yield plateau should also be accounted for since the material properties of hot-rolled steels feature distinct yield plateau with moderate strain hardening rather than the relatively rounded non-linear response of cold-formed steel [28].

$$f_{csm} = \begin{cases} E_s\varepsilon_{csm} & \text{for } \varepsilon_{csm} \le \varepsilon_y \\ f_y & \text{for } \varepsilon_y < \varepsilon_{csm} < \varepsilon_{sh} \\ f_y + E_{sh}(\varepsilon_{csm} - \varepsilon_{sh}) & \text{for } \varepsilon_{sh} < \varepsilon_{csm} < C_1\varepsilon_u \end{cases} \quad (2)$$

$$E_{sh} = \frac{f_u - f_y}{C_2\varepsilon_u - \varepsilon_y} \quad (3)$$

where E_s is Young's modulus, f_y and f_u are the yield and ultimate tensile stress, ε_y and ε_u are the strains at the yield and ultimate stresses, respectively, ε_{sh} is the hardening strain defined as the end of the yield plateau after which the strain hardening initiates, $C_1\varepsilon_u$ represents the strain at the intersection point of the third stage of the model and the actual stress-strain curve. The other material coefficients C_2 is used to define the strain hardening modulus of E_{sh}. The obtained stress-strain curves taken from parent plates are compared with the quad-linear material model applied in CSM, as shown in Fig. 19. Q690 stress-strain curves are accurately re-constructed using the proposed quad-linear model in [40] as shown in Fig. 19(a), whereas the strain hardening of Q460 starts earlier than the predicted hardening strain due to the relatively short yield plateau as presented in Fig. 19(b). It is also worth noting that the quad-linear model proposed in [1] and [40] provides ε_{sh} equal to 0.025 which is larger than the obtained test results at about 0.012. Thus, the modified quad-linear model is adopted in cross-section resistance calculation by shifting the tested curve to the hardening strain at 0.012, as shown in Fig. 19(b) in black dash dot line.

It was observed that in the determination of the cross-section slenderness parameter λ_p, two different strength grades were essentially included in hybrid sections. Thus, the cross-section slenderness parameter was derived based on flange strength from Q690 and web strength of Q460 respectively. Figs. 20–21 present comparisons between two different cross-section slenderness. The current specified slenderness limit value of DSM is unsafe if the cross-section slenderness is determined based on the lower strength grade from the web, whereas the cross-section classification remains on safe side if the slenderness value is determined based on higher strength grade of flange.

Table 10 Summary of EC3, AISC, AS, DSM and CSM slenderness limits between slender and non-slender plate elements in compression.

Design standards and methods	Yield slenderness limits
EN 1993-1-12	$c/t \leqslant 14\varepsilon_{EC3}$
ANSI/AISC 360-16	$c/t \leqslant 0.64\varepsilon_{AISC}$
AS 4100	$c/t \leqslant 14\varepsilon_{AS4100}$
DSM	$\lambda_p = 0.776$
CSM	$\lambda_p = 0.68$

Table 11 CSM material model for HSS materials.

	ε_u	ε_{sh}	C_1	C_2
$f_y/f_u \leqslant 0.85$	$0.6(1-\frac{f_y}{f_u})$	$0.1\frac{f_y}{f_u}-0.055$		
$0.85 < f_y/f_u \leqslant 0.9$	$0.8(1-\frac{f_y}{f_u})$	$0.2\frac{f_y}{f_u}+0.2$	$\frac{\varepsilon_{sh}+0.3(\varepsilon_u-\varepsilon_{sh})}{\varepsilon_u}$	$\frac{\varepsilon_{sh}+0.55(\varepsilon_u-\varepsilon_{sh})}{\varepsilon_u}$
$0.9 < f_y/f_u$	$1-\frac{f_y}{f_u}$	0.02		

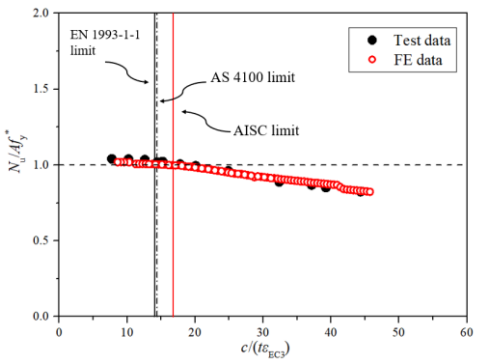

Fig. 18. Assessment of slenderness limit in design codes for outstand flanges of welded section in compression.

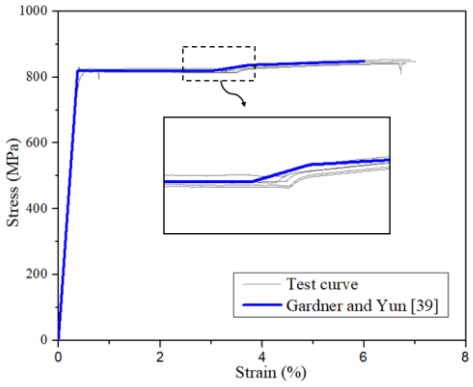

(a)

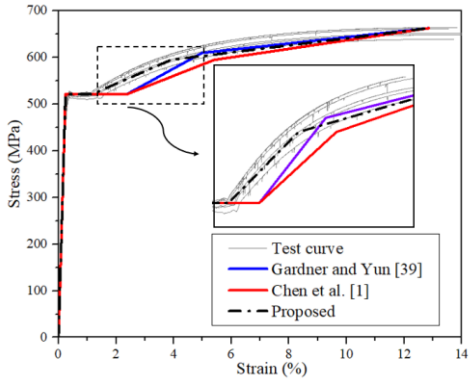

(b)

Fig. 19. Comparison with the experimental stress-strain curves with the proposed material models applied in CSM (a) Comparison of the test Q 690 stress-strain curves with quad-linear model proposed by Yun and Gardner [40] (b) Comparison of the test Q460 stress-strain curves with different models for Q460.

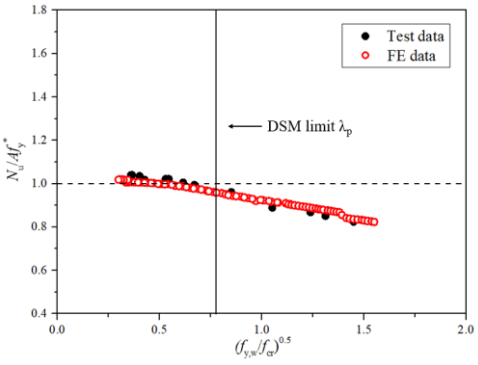

Fig. 20. Assessment of DSM cross section slenderness limit with slenderness obtained based on strength from the web $f_{y,w}$

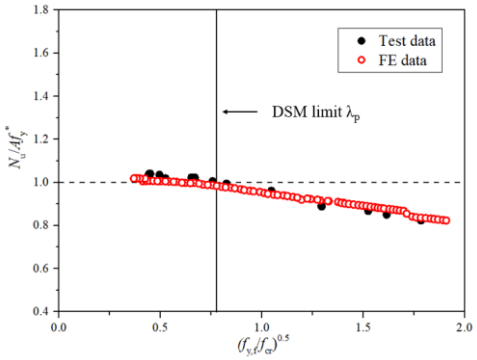

Fig. 21. Assessment of DSM cross section slenderness limit with slenderness obtained based on strength from the flange $f_{y,f}$

4.3 Cross-section compression capacities

Investigation on the compression predictions from the design codes and the design methods were also conducted. Compression predictions derived in accordance with the design codes and the design methods were assessed and evaluated against the experimental and numerical performance data. It should be noted that all these three structural steel design codes stipulate the compression resistance of yield load Af_y for non-slender sections or Class 1-3 sections while effective width method was adopted to deal with the sections with occurrence of buckling prior to reaching the yield load for slender sections or Class 4 counterparts. Note however that the EN 1993-1-12 [17], ANSI/AISC 360-16 [18] and AS 4100 [35] employ different equations to determine the effective width of the Class 4 or slender plate elements subject to local buckling, as given in Eqs. (4) – (6),

$$c_{\text{eff,EC3}} = c\left(\frac{1}{\bar{\lambda}_p} - \frac{0.188}{\bar{\lambda}_p^{\,2}}\right) \le c \tag{4}$$

$$c_{\text{eff,AISC}} = c\left(\frac{1.49\lambda_{\text{p,AISC}}}{c/t} - \frac{0.49\lambda_{\text{p,AISC}}^{\,2}}{(c/t)^2}\right) \le c \tag{5}$$

$$c_{\text{eff,AS4100}} = c\left(\frac{14}{c/(t\varepsilon_{\text{AS4100}})}\right) \le c \tag{6}$$

where $\lambda_{\text{p,AISC}}$ is the AISC limiting width-to-thickness ratio for outstand plate element, and plate element slenderness codified in EN 1993-1-12 [17] can be derived from Eq. (7)

$$\bar{\lambda}_p = \frac{c/t}{28.4\varepsilon_{\text{EC3}}\sqrt{k_\sigma}} \tag{7}$$

where k_σ is the buckling factor taken as 0.43 for outstand plate element in compression.

In terms of the cross-section resistance for DSM, when the cross-section slenderness is larger than 0.776, the

cross-section resistance is derived based on the cross section non-dimensional slenderness, with cross-section capacity determined according to Eq. (8)

$$N_{DSM} = \begin{cases} f_y A & \text{for } \lambda_p \le 0.776 \\ (1-\frac{0.15}{\lambda_p^{0.8}})\frac{1}{\lambda_p^{0.8}} f_y A & \text{for } 0.776 > \lambda_p \end{cases} \quad (8)$$

For cross-section resistance predictions from CSM, the stub column capacity is derived based on the gross cross-section area and the determination of the CSM design stress f_{csm}, as shown in Eq. (9)

$$N_{CSM} = \begin{cases} f_{csm} A & \text{for } \lambda_p \le 0.68 \\ \frac{\varepsilon_{csm}}{\varepsilon_y} f_y A & \text{for } \lambda_p > 0.68 \end{cases} \quad (9)$$

The experimental data in conjunction with the numerical results of hybrid HSS welded T-section stub column specimens were normalized by the design compression capacities predicted from the design codes and predictions derived from DSM and CSM. The normalized strengths are plotted against the corresponding normalized plate slenderness, as shown in Figs. 22 – 28. Table 12 summarizes the results of the statistical analysis of the cross-section resistance predictions, including the mean (test and FE)- to-predicted compression resistance ratios $N_u/N_{u,pred}$, the corresponding coefficient of variations (CoVs). The mean values of $N_u/N_{,pred}$ obtained from EN 1993-1-12, AISC 360-16, AS4100 are 1.06, 1.05 and 1.08 with corresponding CoVs of 0.03, 0.03 and 0.04. Compared with EN 1993-1-12 and AISC 360-16, design code of AS 4100 provides comparatively conservative predictions for hybrid HSS welded T-sections. Both design codes of EN 1993-1-12 and AISC 360-16 yield rather accurate and consistent predictions of cross section compressive resistance which may be extended to cover compressive design of hybrid HSS welded T-section stub columns. In terms of the design method, $N_{u,DSM}^*$ is the compressive resistance calculated based on $\lambda_p = (f_{cr}/f_{y,f})^{0.5}$, where $f_{y,f}$ is the 0.2% proof strength from the flange, and $N_{u,DSM}$ is the compressive resistance calculated based on $\lambda_p = (f_{cr}/f_{y,w})^{0.5}$, where $f_{y,w}$ is the 0.2% proof strength from the web. The mean values of $N_u/N_{,pred}$ obtained from $N_{u,DSM}$ and $N_{u,DSM}^*$ are 1.09 and 1.20 with CoVs of 0.10 and 0.16 respectively. The mean values of $N_u/N_{,pred}$ obtained from $N_{u,CSM}$ and $N_{u,CSM}^*$ are 1.16 and 1.31 with CoVs of 0.15 and 0.21 respectively. It should be noted that classification of DSM that based on lower strength of web $f_{y,f}$ overestimates the strength as many data points on the left side of limits cannot reach the yield load, as shown in Fig. 19. The strength predictions from DSM reasonably provide conservative results as shown in Fig. 25. Note that classification of DSM* that based on higher strength grade of flange $f_{y,f}$ can be safely adopted for classification of hybrid HSS welded T-section, thereby resulting in reliable compressive resistance predictions with noted conservatism particularly for non-compact sections as shown in Fig. 26. The results of the cross-section resistance predictions coincide well with the cross-section classification. Similarly, for strength predictions from CSM and CSM*, over-conservative predictions were obtained from CSM* for slender sections as shown in Fig. 28, and the strength predictions from CSM can be adopted for hybrid T -section stub columns despite exhibited conservatism when approaching the slenderness limits of $\lambda_p = 0.68$ as presented in Fig. 27.

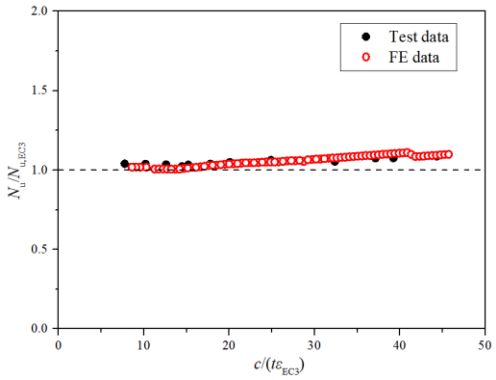

Fig. 22. Comparisons of experimental and numerical results with strength predictions from EC3

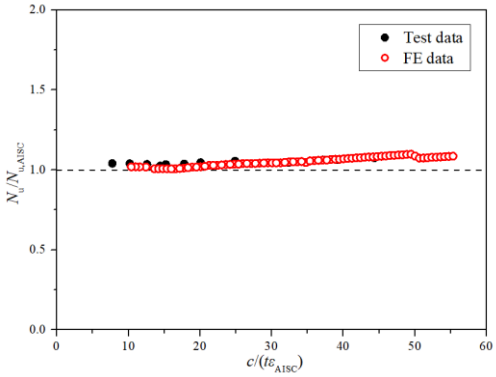

Fig. 23. Comparisons of experimental and numerical results with strength predictions from ANSI/AISC 360-16

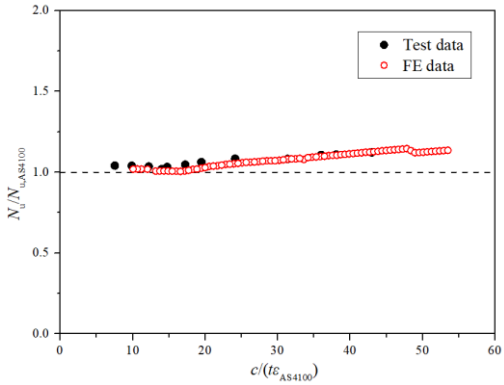

Fig. 24. Comparisons of experimental and numerical results with strength predictions from AS 4100

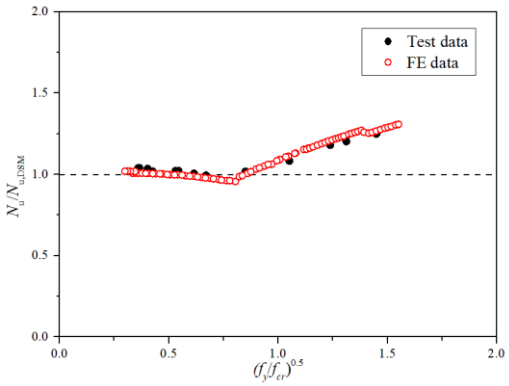

Fig. 25. Comparisons of experimental and numerical results with strength predictions from DSM

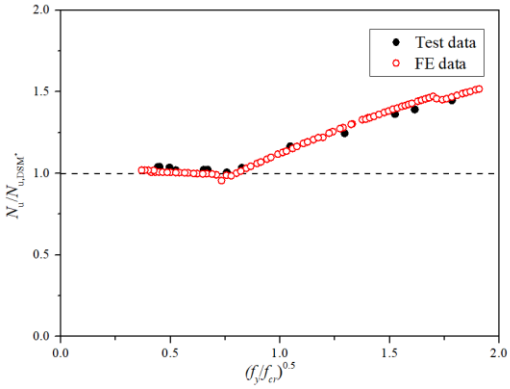

Fig. 26. Comparisons of experimental and numerical results with strength predictions from DSM*

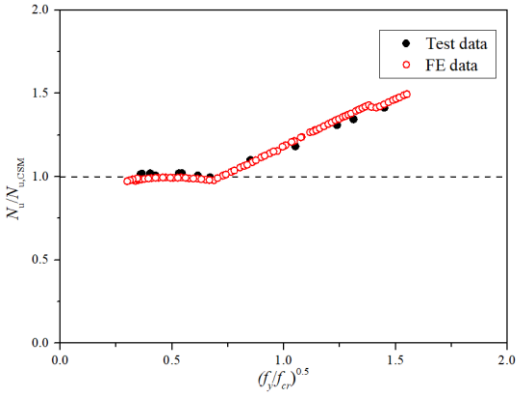

Fig. 27. Comparisons of experimental and numerical results with strength predictions from CSM

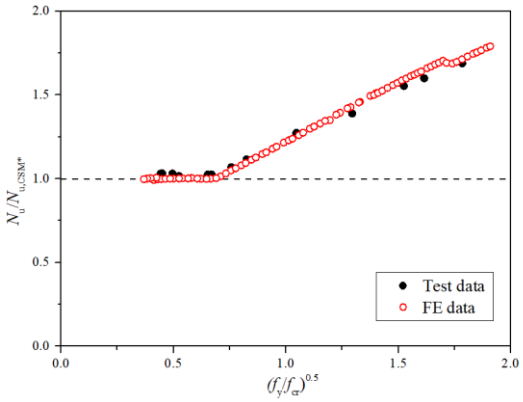

Fig. 28. Comparisons of experimental and numerical results with strength predictions from CSM*

4.4 Reliability analysis

Statistical analysis of the cross-section resistance predictions and the reliability of the design codes as well as the design methods were also conducted. The first-order reliability method in accordance with EN 1990 [44] was conducted to assess the reliability level of the design codes and design methods on hybrid HSS welded T-section stub columns. The coefficients of variations of the basic variables need to be determined based on the prior knowledge. The material over-strength $f_{y,mean}/f_{y,nom}$ = 1.12 based on extensive collated data in [1] was used with CoV of 0.066. The CoV of the geometric properties was taken as 0.05 [41]. The key reliability analysis results are shown in Table 12. In this table, b is the mean value correction factor, which can be derived based on least squares analysis between the resistance capacities and design predictions. V_δ is the CoV of the test and FE results relative to the resistance design model. V_r is the combined CoV incorporating both model and basic variable uncertainties. γ_{M0} is the partial safety factor for cross section resistance. Based on the statistical results in Table 12, it was concluded that design codes of EN 1993-1-12, AISC 360-16 and AS4100 provide consistent and relatively accurate results, despite the required partial safety factor are greater than the suggested 1.0 in EN 1993-1-12 [17] and EN 1993-1-5 [42].

Table 12 Comparisons of test and FE results with predicted strengths.

Number of Specimens		$N_u/N_{u,EC3}$	$N_u/N_{u,AISC}$	$N_u/N_{u,AS4100}$	$N_u/N_{u,DSM}$	$N_u/N_{u,DSM}^*$	$N_u/N_{u,CSM}$	$N_u/N_{u,CSM}^*$
Test:14	FE:76							
	Mean	1.06	1.05	1.08	1.09	1.20	1.16	1.31
	CoV	0.03	0.03	0.04	0.10	0.16	0.15	0.21
	b	1.06	1.06	1.08	1.08	1.17	1.13	1.23
	V_δ	0.03	0.02	0.04	0.10	0.15	0.15	0.21
	V_r	0.09	0.09	0.09	0.14	0.17	0.17	0.22
	γ_{M0}	1.10	1.05	1.05	1.17	1.42	1.32	1.46

5. Conclusions

In this paper, the experimental investigations into the structural behaviour of hybrid HSS welded T-section stub columns have been firstly reported. Subsequently, the developed finite element models were validated against the test results. The validated FE models were used to generate more numerical data to complement the experimental data covering a wider range of cross-section slenderness. Based on the generated structural performance data, the accuracy of the slenderness limits for classifications of outstand plate elements in compression and the local buckling design rules given in EN 1993-1-12, ANSI/AISC 360-16, AS 4100 as well as DSM were assessed. Base on the experimental and numerical results presented in this paper, the following findings can be drawn:

(a) The current codified slenderness limits in EN 1993-1-12, ANSI/AISC 360-16 and AS 4100 for outstand flat elements are generally applicable for hybrid HSS welded T-section under compression.

(b) DSM provides conversative cross-section classification slenderness limits when lower strength grade of web is used.

(c) Consistent cross-section strength predictions are obtained from all three design codes. EN 1993-1-12 and AISC 360-16 generally provide more satisfactory predictions compared with AS 4100.

(d) Compared with CSM, DSM provide relatively accurate strength predictions. CSM provide accurate predictions for compact sections, whereas strengths of slender sections are overly under-estimated.

(e) For cross-section strength prediction from DSM and CSM, the material yield strength $f_{y,w}$ (lower strength) from the web plate may be used rather than the yield strength $f_{y,f}$ (higher strength) from the flange to determine the cross-section slenderness λ_p.

Acknowledgement

The authors would also like to thank the technical staff, Mr. H.Y. Leung, Mr. K.H. Wong of the Structural Engineering Research Laboratory for their support as well as the support from the Industrial Center at The Hong Kong Polytechnic University.

References

[1] S. Chen, H. Fang, J.-Z. Liu, T.-M. Chan, Design for local buckling behaviour of welded high strength steel I-sections under bending, Thin-Walled Struct. 172 (2022) 108792.
[2] F. Nishino, Y. Ueda, L. Tall, Experimental investigation of the buckling of plates with residual stresses, Test methods for compression members, ASTM International1967.
[3] F. Nishino, L. Tall, Experimental investigation of the strength of T-1 steel columns, Fritz Engineering Laboratory, Department of Civil Engineering, Lehigh University1970.
[4] K. Rasmussen, G. Hancock, Design of cold-formed stainless steel tubular members. II: Beams, J. Struct. Eng. 119(8) (1993) 2368-2386.
[5] G. Shi, J. Wang, Y. Bai, Y. Shi, Experimental study on seismic behavior of 460MPa high strength steel box-

754 section columns, Adv Struct Eng 17(7) (2014) 1045-1059.
755 [6] L. Zhang, F. Wang, Y. Liang, O. Zhao, Press-braked S690 high strength steel equal-leg angle and plain
756 channel section stub columns: Testing, numerical simulation and design, Eng. Struc. 201 (2019) 109764.
757 [7] F. Wang, O. Zhao, B. Young, Testing and numerical modelling of S960 ultra-high strength steel angle and
758 channel section stub columns, Eng. Struc. 204 (2020) 109902.
759 [8] X. Cao, L. Gu, Z. Kong, G. Zhao, M. Wang, S.-E. Kim, D. Jia, C. Ma, Local buckling of 800 MPa high
760 strength steel welded T-section columns under axial compression, Eng. Struc. 194 (2019) 196-206.
761 [9] J.-Z. Liu, S. Chen, T.M. Chan, Testing, numerical modelling and design of Q690 high strength steel welded
762 T-section stub columns. Eng. Struc. 259 (2022) 114142.
763 [10] N. Nagarajarao, P. Marek, L. Tall, Welded hybrid steel columns, Welding Journal 51(9) (1972) 4625-4725.
764 [11] R.W. Frost, C.G. Schilling, Behavior of hybrid beams subjected to static loads, J. Struct. Div. 90(3) (1964)
765 55-88.
766 [12] M. Veljkovic, B. Johansson, Design of hybrid steel girders, J. Constr. Steel. Res. 60(3-5) (2004) 535-547.
767 [13] M. Shokouhian, Y. Shi, Flexural strength of hybrid steel I-beams based on slenderness, Eng. Struc. 93
768 (2015) 114-128.
769 [14] M. Ito, K. Nozaka, T. Shirosaki, K. Yamasaki, Experimental study on moment–plastic rotation capacity
770 of hybrid beams, Journal of Bridge Engineering 10(4) (2005) 490-496.
771 [15] C.-S. Wang, L. Duan, Y.F. Chen, S.-C. Wang, Flexural behavior and ductility of hybrid high performance
772 steel I-girders, J. Constr. Steel. Res. 125 (2016) 1-14.
773 [16] H. Bartsch, F. Eyben, G. Pauli, S. Schaffrath, M. Feldmann, Experimental and Numerical Investigations
774 on the Rotation Capacity of High-Strength Steel Beams, J. Struct. Eng. 147(6) (2021) 04021067.
775 [17] EN 1993-1-12, Eurocode 3: Design of Steel Structures – Part 1–12: Additional Rules for the Extension of
776 EN 1993 up to Steel Grades S700, European Committee for Standardization (CEN), Brussels, 2007.
777 [18] ANSI/AISC 360-16, Specification for Structural Steel Buildings, American Institute of Steel Construction
778 (AISC), Chicago, 2016.
779 [19] B. Schafer, T. Peköz, Computational modeling of cold-formed steel: characterizing geometric
780 imperfections and residual stresses, J. Constr. Steel. Res. 47(3) (1998) 193-210.
781 [20] L. Gardner, M. Ashraf, Structural design for non-linear metallic materials, Eng. Struc. 28(6) (2006) 926-
782 934.
783 [21] EN ISO 6892-1, Metallic Materials – Tensile Testing Part 1: Method of Test at Ambient Temperature, EN
784 ISO 6892-1, CEN, Brussels, Belgium, 2019.
785 [22] J.-Z. Liu, H. Fang, S. Chen, T.M. Chan, Material properteis and residual stresses of high strength steel
786 hexagonal hollow sections. J. Constr. Steel. Res. 190 (2022) 107061.
787 [23] H. Fang, T.M. Chan, B. Young, Behavior of Octagonal High-Strength Steel Tubular Stub Columns, J.
788 Struct. Eng. 145(12) (2019) 04019150.
789 [24] J. Chen, J.-Y. Zhu, T.-M. Chan, Experimental and numerical investigation on stub column behaviour of
790 cold-formed octagonal hollow sections, Eng. Struc. 214 (2020) 110669.
791 [25] J.-L. Ma, T.-M. Chan, B. Young, Experimental Investigation on Stub-Column Behavior of Cold-Formed
792 High-Strength Steel Tubular Sections, J. Struct. Eng. 142(5) (2016) 04015174.
793 [26] L. Gardner, D.A. Nethercot, Experiments on stainless steel hollow sections—Part 1: Material and cross-
794 sectional behaviour, J. Constr. Steel. Res. 60(9) (2004) 1291-1318.
795 [27] J. Chen, T.-M. Chan, A.H. Varma, Stub Column Behavior of Cold-Formed High-Strength Steel Circular
796 Hollow Sections under Compression, J. Struct. Eng. 146(12) (2020) 04020277.
797 [28] X. Yun, L. Gardner, N. Boissonnade, The continuous strength method for the design of hot-rolled steel

crosssections, Eng. Struc. 157 (2018) 179-191.
[29] K. Tse, J. Wang, X. Yun, Structural behaviour and continuous strength method design of high strength steel non-slender welded I-section beam-columns, Thin-Walled Struct. 169(3) (2021) 108273.
[30] T.M. Chan, L. Gardner, Compressive resistance of hot-rolled elliptical hollow sections, Eng. Struc. 30(2) (2008) 522-532.
[31] T.-M. Chan, X.-L. Zhao, B. Young, Cross-section classification for cold-formed and built-up high strength carbon and stainless steel tubes under compression, J. Constr. Steel. Res. 106 (2015) 289-295.
[32] J.-Z. Liu, H, Fang, T.-M. Chan, Material properties and residual stresses of high strength steel irregular octagonal hollow sections, J. Constr. Steel. Res. 191 (2022) 107170.
[33] J.-Z. Liu, H, Fang, T.-M. Chan, Investigation on material properties and residual stresses in cold-formed high strength steel irregular hexagonal hollow sections, Thin-Walled Struct. 175 (2022) 109220.
[34] X. Cao, Y. Xu, Z. Kong, H. Shen, W. Zhong, Residual stress of 800 MPa high strength steel welded T section: Experimental study, J. Constr. Steel. Res. 131 (2017) 30-37.
[35] AS 4100-1998(R2016), Steel structures (Reconfirmed 2016 Incorporating Amendment No.1), AS 4100, Australian Standard, Sydney, Australia, 2016.
[36] B.W. Schafer, S. Ádány, Buckling analysis of cold-formed steel members using CUFSM: conventional and constrained finite element strip methods, in: Proceedings of the 18th International Speciaty Conferences on Cold-formed Steel Structures, 2006, 39–54.
[37] ABAQUS/Standard. Version 6.14-1, K. a. S. Hibbit, U.S.A.
[38] AISI S100-16, North American Specification for the Design of Cold-Formed Steel Structural Members, AISI (American Iron and Steel Institute), Washington, DC, USA, 2016.
[39] X. Lan, J. Chen, T.-M. Chan, B. Young, The continuous strength method for the design of high strength steel tubular sections in compression, Eng. Struc. 162 (2018) 177-187.
[40] X. Yun, L. Gardner, Stress-strain curves for hot-rolled steels, J. Constr. Steel. Res. 133 (2017) 36-46.
[41] S. Afshan, P. Francis, N.R. Baddoo, L. Gardner, Reliability analysis of structural stainless steel design provisions, J. Constr. Steel. Res. 114 (2015) 293-304.
[42] EN 1993-1-5, Eurocode 3: Design of Steel Structures – Part 1–5: Plated structural elements. Brussels: European Committee for Standardization (CEN), Brussels, 2006.
[43] L. Kang, Y. Wang, X. Liu, B. Uy, Investigation of residual stresses of hybrid normal and high strength steel (HNHSS) welded box sections, Steel Compos Struct 33(4) (2019) 489-507.
[44] EN 1990. Eurocode - Basis of structural design, European Committee for Standardization (CEN), Brussels, Belgium, 2002.